7-5-2011

# Dynamics of Droplet Motion under Electrowetting Actuation

S. Ravi Annapragada
*Purdue University*, asravi@purdue.edu

Susmita Dash
*Purdue University*, sdash@purdue.edu

Suresh V. Garimella
*Birck Nanotechnology Center, Purdue University*, sureshg@purdue.edu

Jayathi Y. Murthy
*Birck Nanotechnology Center, Purdue University*, jmurthy@purdue.edu

# Dynamics of Droplet Motion under Electrowetting Actuation

S. Ravi Annapragada, Susmita Dash, Suresh V. Garimella,* and Jayathi Y. Murthy

Cooling Technologies Research Center, an NSF IUCRC, School of Mechanical Engineering and Birck Nanotechnology Center, Purdue University, West Lafayette, Indiana 47907-2088, United States

**ABSTRACT:** The static shape of droplets under electrowetting actuation is well understood. The steady-state shape of the droplet is obtained on the basis of the balance of surface tension and electrowetting forces, and the change in the apparent contact angle is well characterized by the Young–Lippmann equation. However, the transient droplet shape behavior when a voltage is suddenly applied across a droplet has received less attention. Additional dynamic frictional forces are at play during this transient process. We present a model to predict this transient behavior of the droplet shape under electrowetting actuation. The droplet shape is modeled using the volume of fluid method. The electrowetting and dynamic frictional forces are included as an effective dynamic contact angle through a force balance at the contact line. The model is used to predict the transient behavior of water droplets on smooth hydrophobic surfaces under electrowetting actuation. The predictions of the transient behavior of droplet shape and contact radius are in excellent agreement with our experimental measurements. The internal fluid motion is explained, and the droplet motion is shown to initiate from the contact line. An approximate mathematical model is also developed to understand the physics of the droplet motion and to describe the overall droplet motion and the contact line velocities.
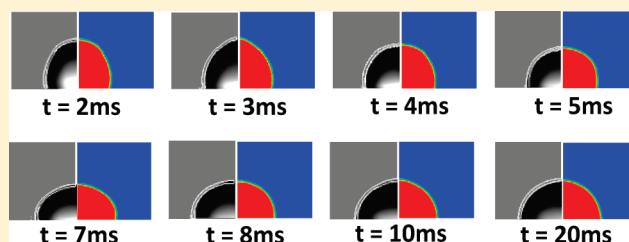
## 1. INTRODUCTION

Droplets are widely encountered in various cooling applications that use electrowetting,[1,2] mist,[3,4] spray,[5] and traditional air conditioning and refrigeration.[6] Emerging cooling techniques such as electrowetting use droplet motion to transport heat.[7,8] A study of droplet dynamics can shed light on the cooling achieved from droplets actuated electrically (or gravitationally). Many microfluidic applications would also benefit from a better understanding of droplet dynamics under electrical actuation.[9−11]

Electrowetting on a dielectric material was first proposed by Berge.[12] Since then, many studies have been conducted to understand the steady-state droplet response to a dc voltage input.[13−16] However, the transient response of the droplet to dc actuation has not been studied in detail and has attracted interest only over the past decade. Blake and Haynes[17] originally proposed a molecular kinetic (MK) theory to predict the motion of the triple contact line. It was shown that for a simplified case the velocity of the contact line is proportional to the difference in the cosines of the apparent contact angle and the intrinsic contact angle. An equivalent contact line force term was developed on the basis of the theory. Blake et al.[18] extended the MK theory to include electrostatic equations along with dynamic wetting to predict the wetting behavior of coated flows on dielectric layers under external electrical actuation forces. Decamps and De Coninck[19] showed the use of this modified MK theory to predict transient electrowetting on the dielectric (EWOD) of droplets. They established that the contact line friction coefficient is independent of voltage. Independently, Schneemilch et al.[20] presented similar results for the case of water droplets on a Parylene dielectric layer. The experimental data also followed the MK theory.

By means of a simple energy balance and comparison with experiments, Ren et al.[21] showed that viscous forces are small when compared to the contact line friction forces during the transient EWOD process. Wang and Jones[22] analyzed the column rise in a modified Pellat experimental apparatus[23] under a step voltage response. A reduced-order model was used to predict the 1D transient height rise of the interface including the contact line friction, which was modeled on the basis of the MK theory. Because it is a simple reduced-order model, its use is limited to column rise predictions.

Sen and Kim[24] observed the contact line motion under a step input but for a coplanar EWOD device. The transient behavior of droplet spreading and the parameters at the contact line were characterized. The time required to reach the maximum contact line speed and its absolute value were predicted on the basis of an order-of-magnitude analysis. Recently, Oh et al.[25] reported the use of shape mode equations to describe the unsteady motion of a sessile drop during dc electrowetting. The model is simplified and is valid for simple EWOD cases and cannot take into account changes in electrode shape and variable thickness.

These studies show that a comprehensive flexible model that predicts transient droplet motion has not been forthcoming. The volume of fluid (VOF) technique provides the framework for such a model. The VOF model has successfully been used to predict droplet statics[26] and dynamics[27] on hydrophobic surfaces under gravitational actuation.

**8198** dx.doi.org/10.1021/la201322b | *Langmuir* 2011, 27, 8198–8204
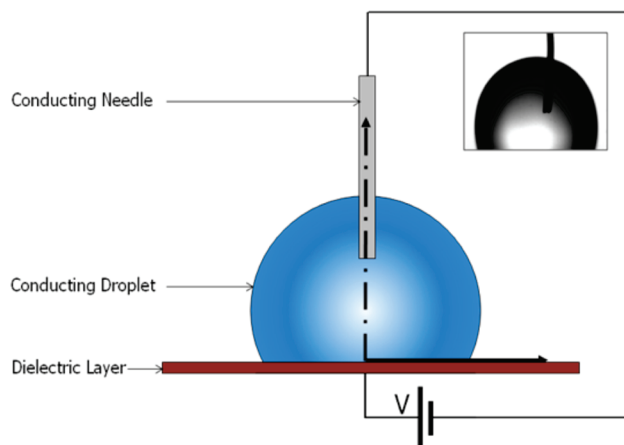
**Figure 1.** Droplet system for transient droplet spreading under electrical actuation. An experimental image of a conducting droplet (water) with a conducting needle is shown in the inset.

Mohseni et al.[28] and Arzpeyma et al.[29] considered electrowetting effects and used VOF to predict the transient shape and linear motion of droplets sandwiched between two parallel electrode arrays. The model was recently improved upon by Keshavarz-Motamed et al.[30] and Rajabi et al.[31] to include the dynamic aspects given by the simplified MK theory as a correction to the static electrowetting contact angle. The dynamic model provided better predictions of droplet dynamics than did the static electrowetting model.

In the present work, we use the contact angle boundary condition of Mohseni et al.[28] using the VOF model to predict the transient, free-surface shape during the spreading of a droplet under the action of electrowetting. A force balance at the contact line is employed, and the droplet motion under a step voltage response is predicted. The time history of the droplet shape, contact line radius, and contact line speeds are computed and compared with measurements from experiments conducted as part of this work for validating the model. The effect of contact line friction on the transient droplet motion is analyzed. An approximate mathematical model is also developed on the basis of the contact line force balance to help interpret the detailed VOF computations. The model is used to predict the transient contact line motion and the maximum contact line velocity. It is found to be in good agreement with experiments and with the detailed VOF model.

## 2. EXPERIMENTAL SETUP

The experimental setup is shown in Figure 1. A conducting droplet is placed on a thin layer of dielectric coated with a Teflon surface and surrounded by air. The experimental droplet response to the applied actuation is recorded at $1000-2000$ fps using a high-speed camera (Photron 1024 PCI). All of the images are processed using MATLAB[32] to determine the dynamic contact angle and the interfacial contact radius. The experimental uncertainties in the contact angle and contact radius measurements are $\pm 2°$ and $\pm 0.03$ mm, respectively.

A highly conducting silicon wafer with a 1-$\mu$m-thick thermally grown oxide layer is utilized as the substrate. The substrate is spin coated with 1% Teflon solution (DuPont, Wilmington, DE) forming a 0.5-$\mu$m-thick later to impart hydrophobicity. An aluminum needle of 125 $\mu$m diameter is inserted into the droplet from the top, as shown in Figure 1. An image of the experimental droplet and the aluminum needle is shown as an inset. A voltage difference is provided between the silicon wafer and the

needle to actuate the droplet. A $5 \pm 0.1$ $\mu$L deionized water droplet is used in all of the experiments. The initial contact angle and the contact radius of the droplet in the absence of electrical actuation are $120 \pm 2°$ and $0.98 \pm 0.03$ mm, respectively.

## 3. NUMERICAL MODEL

In the current work, the volume of the fluid-continuum surface force (VOF-CSF) model in the commercial fluid dynamics software package, FLUENT,[33] is used. A custom contact-angle model based on the force balance at the contact line is implemented using user defined functions to capture the effects of surface tension, electrowetting, and dynamic contact line forces.

**3.1. VOF-CSF Method.** In the VOF method, the flow of noninterpenetrating fluids is simulated by solving a single set of Navier–Stokes equations and tracking the volume fraction of one or more secondary fluids in the domain. The volume fraction of the secondary phase $s$ is obtained by solving the continuity equation for this phase:

$$\frac{\partial}{\partial t}(\alpha_s) + \nabla(\alpha_s \, \vec{v}) = 0 \tag{1}$$

The volume fraction of the primary phase is calculated from

$$\alpha_p + \sum \alpha_s = 1 \tag{2}$$

The shape of the interface is necessary to accurately calculate the advective and diffusive terms of the continuity and momentum equations in the finite volume formulation. For this purpose, Youngs' geometric reconstruction scheme,[34] which is based on a piecewise linear reconstruction of the interface in a partially filled computational cell, is used. Further details of the implementation may be found in the FLUENT manual.[33]

The momentum equation is solved for the average velocity of the mixture, and the influence of multiple phases appears through the phase-fraction-dependent local properties of the material in each cell.

$$\frac{\partial}{\partial t}(\rho \, \vec{v}) + \nabla(\rho \, \vec{v} \, \vec{v})$$
$$= -\nabla p + \nabla[\mu(\nabla \, \vec{v} + \nabla \, \vec{v}^T)] + \rho \, \vec{g} + \vec{F} \tag{3}$$

Here, the gravitational acceleration is specified as $\vec{g} = g \cos \beta + g \sin \beta$, where $\beta$ is the angle of inclination of the surface, as shown in ref 33. Physical properties such as the density and viscosity are volume averaged as follows

$$\rho = \alpha_s \rho_s + (1 - \alpha_s)\rho_p \tag{4}$$

$$\mu = \alpha_s \mu_s + (1 - \alpha_s)\mu_p \tag{5}$$

where subscripts p and s represent the primary and secondary phases, respectively. In the CSF formulation, when only two phases exist, the volumetric force $\vec{F}$ in eq 3 is given by

$$\vec{F} = \sigma \frac{\rho \kappa_s \nabla \alpha_s}{\frac{1}{2}(\rho_p + \rho_s)} \tag{6}$$

where $\sigma$ is the coefficient of surface tension and $\kappa_s$ is the interfacial curvature for the secondary phase, given by Brackbill et al.[35] to be

$$\kappa_s = -(\nabla \cdot \hat{n}) \tag{7}$$

In 7, $\hat{n}$ is the unit vector normal to the free surface. The normal is obtained on the basis of the volume fraction gradient given by

$$n = \frac{\nabla \alpha_s}{|\nabla \alpha_s|} \quad (8)$$

The interface shape at the triple line, where the two phases meet the wall, is imposed by specifying $\hat{n}$ through the specification of the contact angle as

$$\hat{n} = \hat{n}_w \cos(\theta_w) + \hat{t}_w \sin(\theta_w) \quad (9)$$

where $\hat{n}_w$ and $\hat{t}_w$ are the unit vectors normal and tangential to the wall (w) respectively; $\hat{n}_w$ points into the secondary fluid and $\theta_w$ is the contact angle that the interface makes with the wall. In the current model, volume fraction smoothing is used to reduce the spurious velocities at the interface associated with the VOF method.[36,37] Smoothing is performed by averaging the volume fraction on the basis of the neighboring cell volume fractions. However, oversmoothing may result in smearing of the interface to more than two cells. A smoothing relaxation value of 0.25 was found to be optimal.[33]

**3.2. Contact Angle Model Based on the Contact Line Force Balance.** The VOF-CSF model requires contact angles to be specified as a boundary condition; therefore, an accurate specification of the apparent contact angle at the contact line is important. The apparent contact angle is obtained on the basis of a force balance at the triple contact line. The forces acting on the contact line are surface tension, electrowetting, and contact line friction forces. The combined effect of the former two forces gives the electrowetting contact angle ($\theta_e$) given by the Young–Lippmann equation:

$$\cos \theta_e = \cos \theta_0 + \frac{1}{\sigma}\left(\frac{\kappa \varepsilon_0 V^2}{d}\right) \quad (10)$$

Here, $\theta_0$ is the intrinsic contact angle, $\kappa$ is the dielectric constant of the dielectric layer, $\varepsilon_0$ is the permittivity of free space, $V$ is the applied voltage, and $d$ is the dielectric layer thickness. The dynamics of the contact line motion can be understood on the basis of the MK theory, which predicts that the contact line friction force ($F_{CL}$) per unit length acting at the triple contact line is given by

$$F_{CL} = \xi \nu(t) \quad (11)$$

where $\xi$ is the coefficient of friction and $\nu(t)$ is the instantaneous velocity of the contact line. The value of $\xi$ during electrowetting was shown to be independent of voltage by Decamps and De Coninck.[19] The new apparent angle, $\theta_{e,dyn}$, including the contact line friction in the force balance at the contact line, is given by

$$\cos \theta_{e,dyn} = \cos \theta_0 + \frac{1}{\sigma}\left(\frac{\kappa \varepsilon_0 V^2}{d} - \xi \nu(t)\right) \quad (12)$$

The main inputs required for this contact angle model are the intrinsic contact angle $\theta_0$ and the coefficient of contact line friction, $\xi$. The implementation of the contact line friction is similar to that of Keshavarz-Motamed et al.[30]

**3.3. Simulation Setup.** The simulation mimics the experimental setup, which is shown in Figure 1. Because droplet motion is axisymmetric in nature, a 2D axisymmetric VOF computation is performed in FLUENT. A square grid in the $r$–$y$ plane is used. A hemispherical cap of water of the required droplet size is initialized in the domain. Any shape changes due to
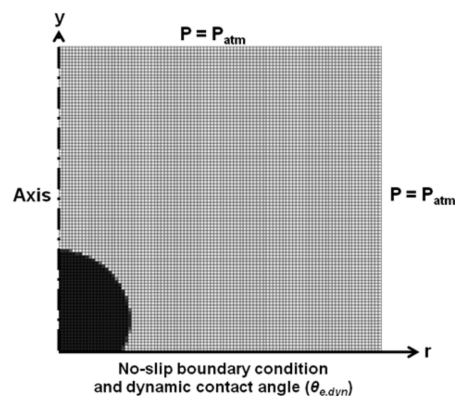


**Figure 2.** Axisymmetric mesh with the initial shape of the droplet (in black).

the presence of the electrode needle at the top of the droplet are neglected. Acceleration due to gravity is applied throughout the domain in the negative $y$ direction. A no-slip boundary condition is specified at the bottom wall. The remaining domain boundaries are specified-pressure boundaries, set at a gauge pressure of zero.[34] The computational domain, mesh, and boundary conditions are shown in Figure 2 along with the initial droplet shape shaded black.

The contact angle model based on the contact line force balance discussed above is implemented as a contact angle boundary condition on the contact line. It is implemented in the VOF-CSF model through user-defined functions (UDFs) in FLUENT.

## 4. RESULTS AND DISCUSSION

In this section, we present results from a simulation of the transient motion of a 5 $\mu$L water droplet on a smooth Teflon surface. The droplet is actuated using different step input voltages. The predictions from the simulations are compared and validated against experiments. The effect of contact line friction on the contact line motion is examined by means of a comparison to computations in which the contact line friction is neglected.

The voltages applied are chosen on the basis of those applied in the experiments using water on a smooth Teflon surface. Voltages of 40, 50, and 60 V are used. Because Lippmann's equation is not valid beyond the saturation voltage (of 65 V), higher voltages are not considered. The water/air surface tension is taken to be 0.072 N/m. The value of $\xi$ is set at 0.4 Ns/m² on the basis of experimental data for the water/Teflon combination from Wang and Jones.[22]

**4.1. Validation.** Figure 3 shows a comparison of the experimental results[32] (left) with the VOF simulation predictions (right) of the time evolution of droplet shape for a step input voltage ($V$ = 60 V). The contour $\alpha_s$ = 0.5 is taken to be the free surface location. Contour lines of $\alpha_s$ = 0.1 and 0.9 (in white) are also superposed on the experimental droplet images to facilitate easier comparison. The contact line is seen to move outward as soon as the voltage is applied. This is due to the change in equilibrium contact angle from 120° at 0 V to 84° at 60 V as predicted by the Lippmann equation (eq 10). The remaining part of the droplet moves to keep the droplet volume constant. This is better visualized through velocity vectors inside the droplet, as shown in Figure 4. The velocity vectors (red) and the droplet
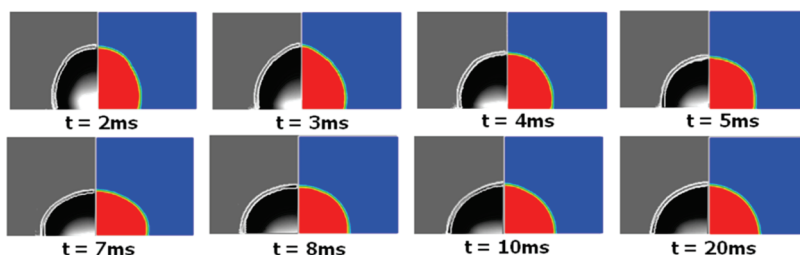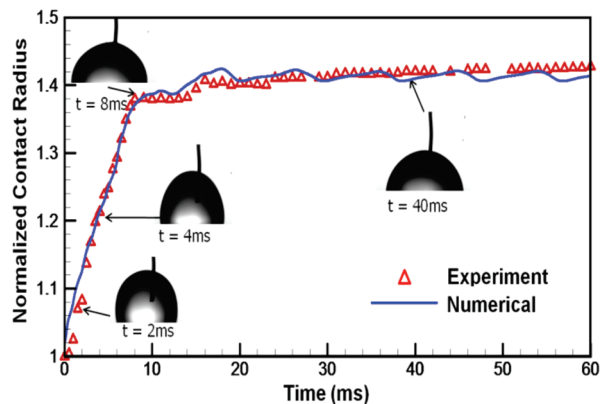
**Figure 3.** Comparison of the computed transient droplet shape with experiments for a step input voltage of 60 V at different instants in time. Gray (left): experimental results. Color (right): simulation results (red, water; blue, air). The contour lines for $\alpha_s = 0.1$ and 0.9 (in white) are superposed on the experimental images.
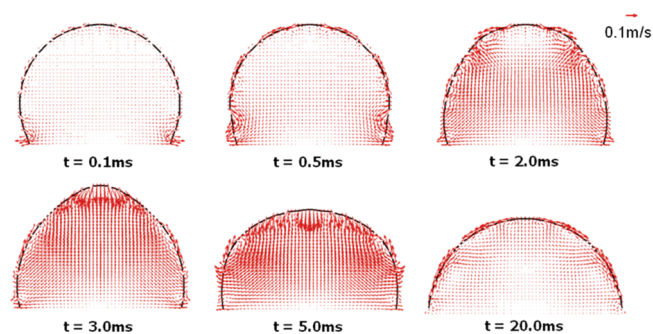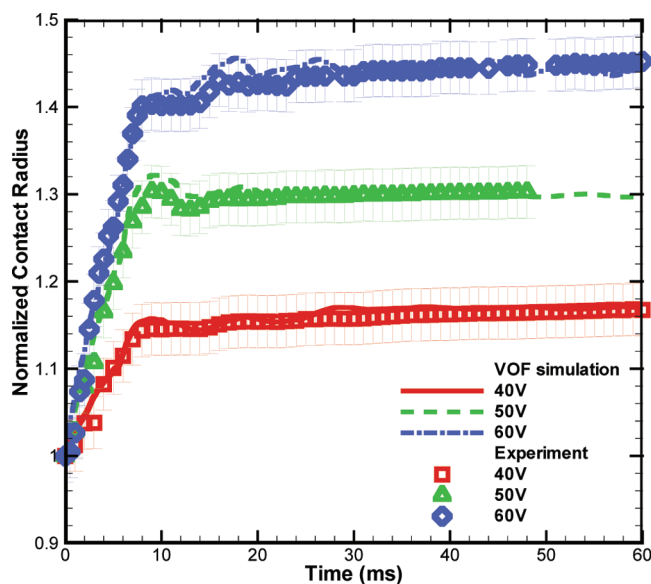


**Figure 4.** VOF simulations of the velocity vectors (in red) and droplet shape (in black) for a step input voltage of 60 V at different instants in time.



**Figure 5.** Comparison of the computed time evolution of the normalized contact radius with experiments for a step input voltage of 60 V.



**Figure 6.** Time history of the normalized contact line radius for different step input voltages (40, 50, and 60 V).

shape (black) are shown at different instants in time. The droplet motion originates at the contact line with high velocities around the region at $t = 0.1$ ms, and the rest of the fluid inside the droplet remains stationary. As time progresses to $t = 2$ ms, more bulk fluid and the remaining interface participate in the motion of the droplet. At $t = 3$ ms, the ripple reaches the top of the droplet and the height of the droplet starts to decrease. This is marked by high velocities at the top of the droplet. The process continues through $t = 5$ ms. At $t = 20$ ms, the velocities inside the droplet die down and the droplet reaches its equilibrium shape.

The time evolution of normalized droplet contact radius is shown in Figure 5. The contact radius is normalized on the basis of the initial contact line radius (before the application of voltage).

The contact line accelerates from a stationary state to a constant velocity; the velocity then slowly goes to zero as the droplet reaches maximum spreading ($r_{CL}$) at around 8 ms. The initial rise in velocity is not seen in the experiments because of small capture rates. Similar transient contact radius behavior is reported by Oh et al.[25] and Wang and Jones.[22] The presence of oscillations is less pronounced in the experiments than in the simulations because of damping by contact angle hysteresis. The computed and experimental time histories of the contact line radius for step voltages of 40, 50, and 60 V are compared in Figure 6. The uncertainty of the length measurement in the experiments ($\pm 0.03$ mm) is shown as error bars in the Figure. The agreement is reasonable, and predictions of the contact line radius fall within experimental error bands. The maximum spreading and the time required to attain it are accurately predicted by the model. The predicted droplet shapes also match reasonably well (Figure 3). The experimental droplet images lie in between the $\alpha_s = 0.1$ and 0.9 contour lines obtained from the numerical solution, validating the numerical methodology. However, because of the asymmetry of the needle, as seen in the insets of Figures 1 and 5, some of the droplets are seen to have nonaxisymmetric shapes.

**4.2. Damping Time.** The predicted time history of the normalized height of the droplet and the contact radius are shown in Figure 7. The contact radius and height are normalized
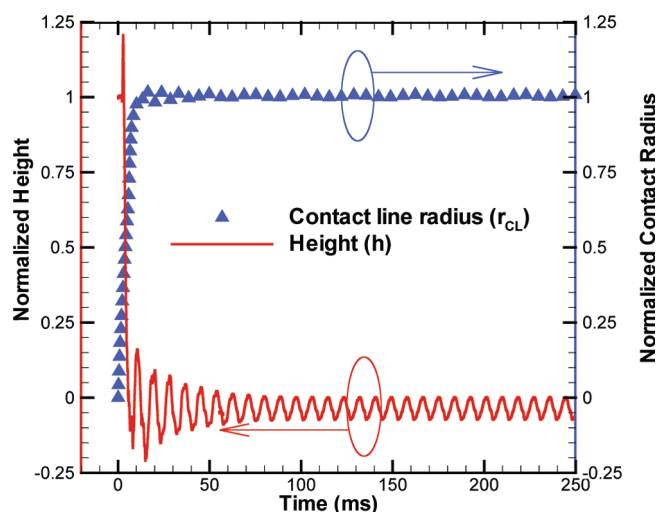
**Figure 7.** Time history of the normalized height and contact line radius from the VOF simulations for a step voltage of $V = 60$ V.



**Figure 8.** Comparison of the computed (with contact line friction, —; without contact line friction, - - -) and experimental time evolution of the normalized contact radius for a step input voltage of 60 V.

on the basis of the initial and final states given by $(r - r_{t=0\,\text{ms}})/(r - r_{t=50\,\text{ms}})$ and $(h - h_{t=50\,\text{ms}})/(h - h_{t=0\,\text{ms}})$, respectively. The contact radius reaches an equilibrium value within 10 ms, whereas the height does not reach its equilibrium value within the entire simulation time of 250 ms. This can be understood by looking at the dominant damping mechanism for the contact radius and height oscillations. The damping mechanism for the contact radius oscillation is dominated by the contact line friction, whereas for the height, it is purely viscous dissipation. The ratio of the time constants for the damping processes are inversely related to the value of the damping constants, which for the case of the contact radius and height are the contact line friction coefficient and the droplet liquid viscosity, respectively. Hence, the ratio of the damping time constants for the height and contact radius is $\tau_\text{h}/\tau_\text{CL} \approx \zeta/\mu_\text{water} = 0.4\,\text{N s m}^{-2}/0.001\,\text{N s m}^{-2} = 400$. The time constant for the oscillation of droplet height is approximately 4 s. This explains why the oscillations in height are not damped out even after 250 ms has elapsed.

**4.3. Effect of Contact Line Friction.** The time histories of the predicted contact line radius with (solid line) and without (dashed line) the contact line friction are shown (Figure 8) for a step input voltage (60 V) along with the experimental measurements (symbols). The absence of contact line friction causes a far larger amplitude of oscillation than is seen in the experiment. The time required to reach equilibrium also exceeds the experimental value by over 2 orders of magnitude. These results indicate that contact line friction dominates viscous damping during the transient spreading of the droplet. A similar conclusion was reached by Wang and Jones[22] in the case of transient capillary rise experiments.

**4.4. Approximate Mathematical Model.** A simplified mathematical model is developed to understand the transient radial motion of the droplet contact line. The major horizontal forces acting on the contact line (i.e., surface tension forces, the electrowetting force, and contact line friction) are included in the model. Viscous forces are neglected becauase they are small compared to these forces.[21] The droplet is assumed to be well described by the spherical cap assumption[26] during transient motion. This is a valid assumption because the Bond number is small ($Bo = 0.17$). However, the nonspherical shapes observed at
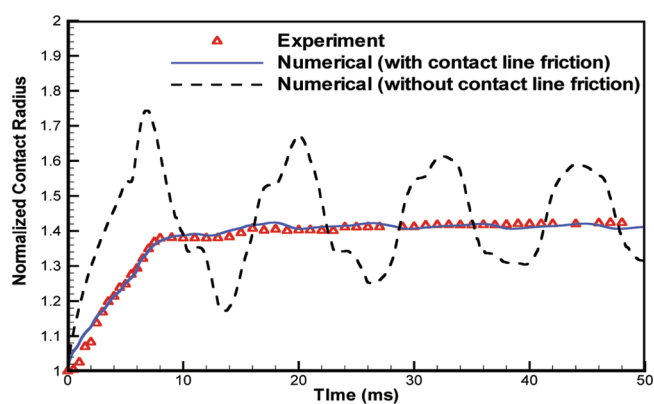
$t = 2.0$ and 3.0 ms in Figure 4 would not be captured by this assumption. When the droplet contact line is in quasi-static equilibrium, the radial forces acting at the contact line are balanced and the droplet transport is governed by

$$\sigma(\cos\theta - \cos\theta_0) - \xi r' + \frac{1}{2}\left(\frac{\kappa\varepsilon_0 V^2}{d}\right) = 0 \qquad (13)$$

which is a reformulation of eq 12. Here, $\theta$ is the instantaneous contact angle and $r'$ is the instantaneous velocity. Under nonequilibrium conditions, the droplet transport equation is obtained by equating the radial force imbalance at the contact line to the rate of change of radial momentum and is given by

$$(m_\text{r} r')' = -\xi r' - \sigma\cos\theta + \left(\sigma\cos\theta_0 + \frac{1}{2}\left(\frac{\kappa\varepsilon_0 V^2}{d}\right)\right) \qquad (14)$$

The instantaneous effective mass ($m_\text{r}$) involved in the droplet motion is taken to be the mass displaced from the original droplet shape shown in Figure 9 and is given by

$$m_\text{r}(r, \theta) = \left(r^2(-4 + \cos(\theta))\cos(\theta)\sin(\theta_0)^2 + (-4 + \cos^2(\theta_0))\sin^2(\theta)r_0^2 \right.$$
$$\left. + 2rr_0(-2 + (-2 + \cos(\theta))\cos(\theta_0)\sin(\theta)\sin(\theta_0)\right)$$
$$\times \frac{\rho}{24r}\left(\frac{[r\cos(\theta)\sin(\theta_0) + (-2 + \cos(\theta))\sin(\theta)r_0]^2}{(\sin^3(\theta)\sin^3(\theta_0)[r(-1 + \cos(\theta))\sin(\theta_0) + (-1 + \cos(\theta_0))\sin(\theta)r_0])}\right) \qquad (15)$$

The droplet contact radius ($r$) and the contact angle ($\theta$) are related through the conservation of volume, $\forall$:

$$\forall = \frac{\pi r^3}{3}\frac{2 - 3\cos\theta + \cos^3\theta}{\sin^3\theta} \qquad (16)$$

This assumes that the remaining mass does not move in the horizontal direction at this instant.

The radial momentum equation (eq 14) is a second-order ordinary differential equation. It is discretized using the finite
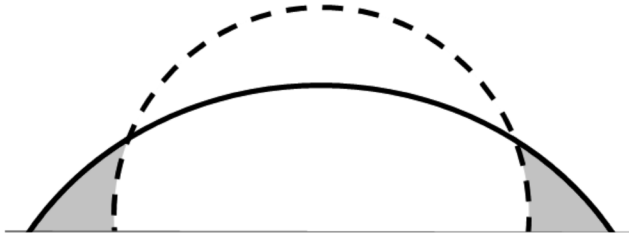
**Figure 9.** Effective mass involved in the droplet motion (gray region). The original droplet shape is shown by a dashed line, and the droplet shape at the current time is shown by a solid line.
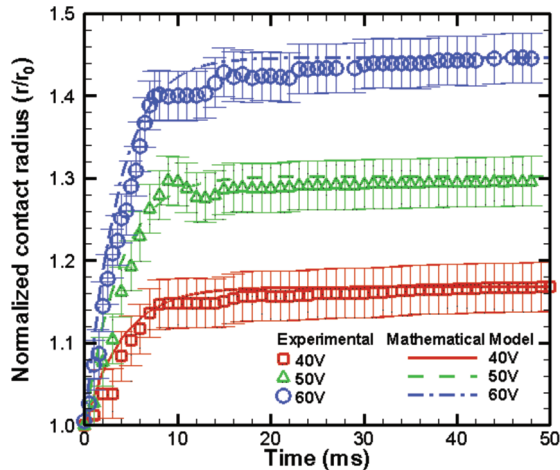


**Figure 10.** Time history of the normalized contact line radius obtained from the approximate mathematical model for different step input voltages (40, 50, and 60 V) compared to experimental values.

difference method with an explicit time marching scheme for $r_n$

$$r^n = r^{n-1} + \frac{m_r^{n-1}(r'^{n-1}\Delta t) - \sigma(\cos(\theta_r^{n-1}) - \cos(\theta_e))\Delta t^2}{m_r^{n-1}r + \left(\zeta + \dfrac{\dfrac{\mathrm{d}m_r^{n-1}}{\mathrm{d}r}(r'^{n-1})^2}{\Delta t}\right)\Delta t}$$

$$(17)$$

Here, $\Delta t$ is the time step, $r'$ is the velocity of the contact line, and $\theta_e$ is the Lippman contact angle. The value of the radius at the previous time level is denoted by $r_{n-1}$, and the contact line velocity is denoted by $r'_{n-1}$. The initial condition for time marching is given by

$$r_0 = \left[\frac{3 \,\forall\, \sin^3\theta_0}{\pi(2 - 3\cos\theta_0 + \cos^3\theta_0)}\right]^{1/3}$$

$$(18)$$

$$r'_0 = \frac{\left(\dfrac{\kappa\varepsilon_0 V^2}{2d}\right)}{\zeta}$$

The initial velocity condition is derived from eq 13 by setting the inertial term on the LHS to zero. This is justified because the instantaneous effective mass at $t = 0$ s is zero. The model is used
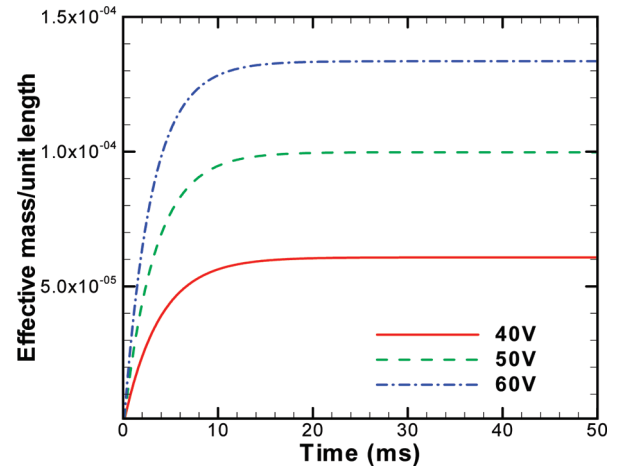


**Figure 11.** Time history of the effective mass per unit radial length for different step input voltages obtained with the approximate mathematical model.

to predict the droplet behavior seen in the experiments. Time-step-independent results were achieved for time steps smaller than $\Delta t = 0.1$ ms.

The material properties and contact line friction coefficient from the volume of fluid simulations are used in the mathematical model. The contact radius time history obtained from the mathematical model is compared with the experimental results (Figure 10) for different step input voltages. The mathematical model accurately predicts the overall trend in the droplet contact line behavior. However, because the droplet does not allow for nonspherical droplet shapes, the additional motion due to the surface waves on the interface is not captured by the mathematical model.

The maximum contact line velocity occurs at $t = 0$ according to the mathematical model and is given by

$$r'_{max} = \frac{\left(\dfrac{\kappa\varepsilon_0 V^2}{2d}\right)}{\zeta}$$

$$(19)$$

The $r'_{max}$ value shows quadratic growth with the step voltage input, which contradicts the predictions from Sen and Kim,[24] who found a linear voltage dependence. Sen and Kim[24] considered the droplet to be dominated by inertial motion and frictional forces were neglected, which results in a discrepancy with our predictions. In the present model, the effective mass involved in the beginning of the simulation is negligible and hence the inertial force is small compared to the frictional forces, as can be seen from the time history of the effective mass (Figure 11). This is also supported by the velocity vectors at $t = 0.1$ ms (Figure 4), which show high velocities at the contact line, with the rest of the fluid remaining stationary. Hence, the main retarding force due to high contact line velocities is the contact line friction given by $F_{CL} = \zeta r'$. The actuation forces acting on the droplet in the early stages go as $F_A \propto V^2$. After these forces are balanced, the contact line velocity shows a quadratic dependence (eq 19) on voltage. The predictions are further validated by comparing them against the detailed numerical predictions and are tabulated in Table 1, showing good agreement.

**Table 1. Comparison of the Predicted Maximum Contact Line Speeds Using the Detailed Numerical Predictions and the Approximate Mathematical Model**

|  | 40 V | 50 V | 60 V |
| --- | --- | --- | --- |
| VOF | 40 mm/s | 68 mm/s | 105 mm/s |
| approximate mathematical model | 38 mm/s | 72 mm/s | 110 mm/s |

## 5. CONCLUSIONS

A generalized numerical model to predict the transient behavior of the droplet shape under electrowetting actuation is formulated and implemented in a VOF framework. The electrowetting and dynamic frictional forces are included as an effective dynamic contact angle through a force balance at the contact line. The model is accurately able to predict the transient behavior of water droplets on smooth hydrophobic surfaces with a dielectric layer below, under a step voltage input. The predictions of the time history of the droplet shape and contact radius are in good agreement with experiments conducted for model validation. The contact line frictional force is shown to be the dominant damping force during the transient process. The droplet motion is shown to originate at the contact line.

An approximate mathematical model is developed to describe the transient droplet dynamics and to understand the governing phenomena. The effective mass involved in the horizontal droplet motion is taken to be the mass displaced from the original droplet shape. The simplified model adequately predicts the general behavior of the droplet motion. The maximum contact line velocities are also accurately predicted.

## ■ AUTHOR INFORMATION

**Corresponding Author**
*E-mail: sureshg@purdue.edu.

## ■ ACKNOWLEDGMENT

## ■ REFERENCES

(1) Bahadur, V.; Garimella, S. V. *J. Micromech. Microeng.* **2006**, *16*, 1494.

(2) Kumari, N.; Bahadur, V.; Garimella, S. V. *J. Micromech. Microeng.* **2008**, *18*, 085018.

(3) Wang, T.; Gaddis, J. L.; Li, X. *Int. J. Heat Mass Transfer* **2005**, *48*, 5179–5191.

(4) Kumari, N.; Bahadur, V.; Hodes, M.; Salamon, T.; Kolodner, P.; Lyons, A.; Garimella, S. V. *Int. J. Heat Mass Transfer* **2010**, *53*, 3346–3356.

(5) Freund, S.; Pautsch, A. G.; Shedd, T. A.; Kabelac, S. *Int. J. Heat Mass Transfer* **2007**, *50*, 1953–1962.

(6) Graham, C.; Griffith, P. *Int. J. Heat Mass Transfer* **1973**, *16*, 337–346.

(7) Bahadur, V.; Garimella, S. V. *Microelectron. J.* **2008**, *39*, 957–965.

(8) Baird, E.; Mohseni, K. *IEEE Trans. Compon. Packag. Technol.* **2008**, *31*, 143–151.

(9) Graham-Rowe, D. *Nat. Photon* **2006**, 2–4.

(10) Srinivasan, V.; Pamula, V. K.; Fair, R. B. *Lab Chip* **2004**, *4*, 310–315.

(11) Hayes, R. A.; Feenstra, B. J. *Nature* **2003**, *425*, 383–385.

(12) Berge, B. *C. R. Acad. Sci., Ser. II: Mec., Phys., Chim., Sci. Terre Univers* **1993**, *317*, 157–163.

(13) Kumari, N.; Bahadur, V.; Garimella, S. V. *J. Micromech. Microeng.* **2008**, *18*, 105015.

(14) Buehrle, J.; Herminghaus, S.; Mugele, F. *Phys. Rev. Lett.* **2003**, *91*, 086101.

(15) Mugele, F.; Buehrle, J. *J. Phys.: Condens. Matter* **2007**, *19*, 375112.

(16) Kang, K. H. *Langmuir* **2002**, *18*, 10318–10322.

(17) Blake, T. D.; Haynes, J. M. *J. Colloid Interface Sci.* **1969**, *30*, 421.

(18) Blake, T. D.; Clarke, A.; Stattersfield, E. H. *Langmuir* **2000**, *16*, 2928–2935.

(19) Decamps, C.; De Coninck, J. *Langmuir* **2000**, *16*, 10150–10153.

(20) Schneemilch, M.; Welters, W. J. J.; Hayes, R. A.; Ralston, J. *Langmuir* **2000**, *16*, 2924–2927.

(21) Ren, H.; Fair, R. B.; Pollack, M. G.; Shaughnessy, E. *Sens. Actuators, B* **2002**, *87*, 201–206.

(22) Wang, K.-L.; Jones, T. B. *Langmuir* **2005**, *21*, 4211–4217.

(23) Jones, T. B., Jr.; Melcher, J. R. *Phys. Fluids* **1973**, *16*, 393.

(24) Sen, P.; Kim, C. *Langmuir* **2009**, *25*, 4302–4305.

(25) Oh, J. M.; Ko, S. H.; Kang, K. H. *Phys. Fluids* **2010**, *22*, 032002–10.

(26) Annapragada, S. R.; Murthy, J. Y.; Garimella, S. V. *Int. J. Heat Mass Transfer* **2011**, in press.

(27) Annapragada, S. R.; Murthy, J. Y.; Garimella, S. V. *Int. J. Heat Mass Transfer* **2011**, in press.

(28) Mohseni, K.; Arzpeyma, A.; Dolatabadi, A. *Can. J. Chem. Eng.* **2006**, *84*, 17–21.

(29) Arzpeyma, A.; Bhaseen, S.; Dolatabadi, A.; Wood-Adams, P. *Colloids Surf., A* **2008**, *323*, 28–35.

(30) Keshavarz-Motamed, Z.; Kadem, L.; Dolatabadi, A. *Microfluid. Nanofluid.* **2010**, *8*, 47–56.

(31) Rajabi, N.; Dolatabadi, A. *Colloids Surf., A* **2010**, *365*, 230–236.

(32) *MATLAB Reference Manual*; The Mathworks, Inc.: Natick, MA, 2007.

(33) *Fluent 6.3 Users' Guide*; Ansys Inc.: Lebanon, NH, 1996.

(34) Youngs, D. L. *Numer. Methods Fluid Dyn. VII, (Proc. Int. Conf.), 7th* **1982**, *1*, 41–51.

(35) Brackbill, J. U.; Kothe, D. B.; Zemach, C. *J. Comput. Phys.* **1992**, *100*, 335–354.

(36) Hardt, S.; Wondra, F. *J. Comput. Phys.* **2008**, *227*, 5871–5895.

(37) Lafaurie, B.; Nardone, C.; Scardovelli, R.; Zaleski, S.; Zanetti, G. *J. Comput. Phys.* **1994**, *113*, 134–147.